European Journal of Computational Mechanics, 2013
Vol. 22, No. 1, 30–58, http://dx.doi.org/10.1080/17797179.2012.751782

Taylor & Francis
Taylor & Francis Group

Elastic foam compression in a finite element (FE) context

K. Hitti*, T. Coupez, M. Bernacki and L. Silva

MINES ParisTech, CEMEF – Centre de Mise en Forme des Matériaux, CNRS UMR 7635, BP 2071 rue Claude Daunesse 06904, Sophia Antipolis Cedex, France

A procedure to generate statistical virtual representative volume elements of foam in a finite element context is described. This technique, based on Laguerre tessellations and advancing front method, level-set description of interfaces and anisotropic meshing adaptation, is detailed. The capability of the procedure to respect statistical data could be insured by the advancing front method. To simulate biaxial foam compression, a uniform velocity is imposed on the domain's upper and lower boundaries. By considering the presence of air inside the foam's cells which are bounded by the elastic solid skeleton, a fluid–structure interaction problem occurs between a compressible elastic solid and a compressible fluid. A monolithic formulation is used for solving this problem. Such strategy gives rise to an extra stress tensor in the Navier–Stokes equations coming from the presence of the structure in the fluid.

Une méthode pour générer des Volumes Elémentaires Représentatifs (VERs) virtuels statistiques de mousse dans un contexte éléments finis (EF) est décrite. Cette technique, basée sur des cellules de Laguerre associée à une méthode frontale de génération, une description des interfaces par des fonctions level-set et une adaptation anisotrope des maillages EF, est détaillée. La capacité de la procédure pour respecter des données statistiques est assurée par la méthode de génération frontale. Pour simuler la compression biaxiale de mousses, une vitesse uniforme est imposée aux frontières supérieure et inférieure du domaine. En considérant la présence de l'air à l'intérieur des cellules de la mousse qui sont limitées par le squelette solide élastique, un problème d'Interaction Fluide Structure (IFS) se produit entre un solide élastique compressible et un fluide compressible. Une formulation monolithique est utilisée pour résoudre se problème. Une telle stratégie induit l'existence d'un tenseur d'extra-contrainte dans les équations de Navier-Stokes.

Keywords: elastic foam; compression; level-set; anisotropic mesh adaptation; finite element method

Mots-clés: mousse élastique; compression; level-set; adaptation anisotrope de maillages; méthode des éléments finis

1. Introduction

Polymer foams are present in our everyday life under diverse forms and functions. They serve, for example, in the manufacturing of mattresses, car bumpers, in the heat or phonic insulation, etc. (an extensive review may be found in (Gibson & Ashby, 1997)). Two-dimensional foams, also referred as Voronoï honeycombs, can appear under regular (hexagonal) and irregular shapes. Three-dimensional foams, which are either closed-cell or open-cell, also appear under regular (cubic or tetradecahedron) and irregular forms. The Voronoï tessellation

*Corresponding author. Email: karim.hitti@mines-paristech.fr

method (VTM) is the most widely used to model these types of microstructures (Zhu, Hobdell, & Windle, 2000; Zhu, Hobdell, & Windle, 2001; Zhu, Thorpe, & Windle, 2006; Zhu & Windle, 2002). We propose to use an implicit method to define these tessellations, i.e. the immersed volume method (Hitti, 2011). This method is based on the level-set approach to define the different interfaces, on mixing laws and on meshing adaptation. The use of level-set functions to define Voronoï cells was introduced by Bernacki, Resk, Coupez, and Logé, (2009). This approach was applied successfully for the generation of 2D or 3D polycrystals. A disadvantage of the VTM is its incapability of respecting a cell size distribution (Xu & Li, 2009). Hence, the Laguerre tessellation method (LTM) (Imai, Iri, & Murota, 1985) is used. Moreover, a simple cell spreading technique is used for defining the foam's solid skeleton. Furthermore, description of representative volume element (RVE)s using a level-set framework undermines the necessity to work with a fine mesh at its interfaces not only to describe properly the considered microstructure but also to take into account discontinuities of physical properties when mechanical testing is performed.

On the other hand, analytical or numerical calculations have been performed on idealised microstructures constructed from a repeating unit cell. Structural mechanics have been applied to open-cell foams schematised either by a regular tetrahedral arrangement of beams (Marchi & Mortensen, 2001; Warren & Kraynik, 1988) or by a regular arrangement of tetrakaidecahedral cells (Warren & Kraynik, 1997; Zhu, Mills, & Knott, 1997) or by the Kelvin cell model (Jang, Kraynik, & Kyriakides, 2008; Mills, 2007). In the case of closed-cell structures, finite element (FE) calculations on tetrakaidecahedral unit cell have also been derived (Mills & Zhu, 1999; Simone & Gibson, 1998). All these approaches lead to similar scaling laws for modulus or strength. They give quite fair estimations of modulus and strength though discrepancies are observed with experimental values. These discrepancies can be attributed to the fact that the perfectly ordered and symmetric microstructures are clearly an oversimplification to the actual perturbed architecture observed in the materials (Jang et al., 2008). Modelling foams using X-ray computed tomography can be an answer to reproduce the real microstructure and use it in FE simulations as in Wismans, Govaert, & van Dommelen (2010) and Wismans, van Dommelen, Govaert, & Meijer (2010) where it was used to model polymeric open-cell foams. In these works, the reconstructed data was segmented and automatically converted into a tetrahedron-based FE model, and also 2D FE models were constructed by taking random slices of the 3D models. Uniaxial compression was performed on the constructed FE models, and the typical deformation mechanisms such as bending and buckling were present in both experiments and FE results. Another possible solution, when real images are not used, is the introduction of different kinds of imperfections or defects to the constructed microstructure to try to explain the experimental discrepancies. In this context, Zhu and co-workers studied the effect of cell irregularity on the high strain compression and elastic properties of 2D Voronoï honeycombs (Zhu et al., 2001,2006) and open-cell foams (Zhu et al., 2000; Zhu & Windle, 2002). They concluded that, for both kinds of foams, a more irregular foam has a higher tangential modulus at low strain but supports a lower compressive stress at higher strain when compared with a more regular one, and the more irregular the random foams, the larger will be their effective Young's modulus and shear modulus, and the smaller will be their bulk modulus. Li et al. studied the effects of cell shape and cell wall thickness variations on the elastic properties of two-dimensional cellular solids (Li, Gao, & Subhash, 2005) and open-cell foams (Li, Gao, & Subhash, 2006). Their simulations indicate that the Young's and shear moduli increase as cell shapes become more irregular (which is coherent with the results described in Zhu et al. (2000, 2001)), but decrease as cell wall thickness gets less uniform. The effects of cell irregularity, relative density and the shape of the strut cross section on the high strain compression of open-cell foams were studied in Zhang & Lu (2007). The

cell irregularity was found to have a similar effect as in Zhu & Windle (2002) and the strut cross section and relative density were found to have great effects on the compressive strength of open-cell foam.

In the above-cited cases, the presence of the air inside the foam's cells was never taken into account though its presence may affect the foam's behaviour. We intend to study the effect of cell irregularity on the strain compression of Voronoï honeycombs while considering the existence of air inside the cells. By taking the air's presence into account, the foam compression becomes a fluid–structure interaction (FSI) problem between the air and the foam's solid skeleton. During the FSI, the pressure and the viscous stress of the fluid act on the solid boundary and lead to structural deformations, which in turn affect the fluid's behaviour and consequently the velocity, pressure and viscous stress of the fluid. Thus, the response of the system can only be determined precisely if the coupled problem is solved. In the standard approach for simulating FSI problems, the solid's equations are solved for the displacement while the fluid's equations provide the velocity and pressure. We begin by writing the momentum and continuity equations and then, by using the behaviour laws of the fluid and solid parts and using specific mixture laws, the final FSI system is obtained. This system is governed by the Stokes equations (when the gravity and inertia effects are neglected) with an extra stress tensor coming from the presence of the structure in the fluid. These equations are solved by a mixed FE method with a P1 + /P1 interpolation, and a Lagrangian framework is used in order to simulate foam compression. In this case, each node remains in coincidence with the same phase throughout the whole deformation process. In particular, the nodes located at the interface of the solid skeleton remains on its boundary during the whole simulation and hence, tracking a moving interface does not present major difficulties. Since, the air's pressure increases rapidly during compression, reaching high compressive strains presents major difficulties because the cells tend to explode and their solid skeleton tends to fracture at high strain rates, especially for irregular foams, and we did not deal with such cases in this work.

This paper is organised as follows. Section 2 is dedicated to the RVEs generation method where we detail the use of level-set functions to define the RVEs, and also the ability of our methods to respect statistical data is discussed. A general overview of the existing mesh adaptation techniques and an improvement of an existing technique is detailed in Section 3. The FE formulation of the FSI problem and the foam compression simulations are detailed in Section 4. Finally, the last section is dedicated to the conclusion.

All numerical calculations mentioned in this paper were performed with the CimLib finite element C++ library developed at CEMEF (Digonnet, Silva, & Coupez, 2007).

2. Microstructure generation

Figure 1 illustrates the procedure to create a virtual microstructure made of Voronoï cells with the associated FE mesh and Delaunay triangulation. The Voronoï tessellation is fully described by N_C seeds or Voronoï nuclei which are also the nodes of the Delaunay triangulation, the dual of the Voronoï tessellation. Each nucleus S_i defines a Voronoï cell C_i, which consists of all points closer to S_i than to any other nucleus. The location of the interfaces is implicitly defined, thanks to a level-set framework. For each individual cell, a signed distance function ϕ, defined over the domain Ω, gives at any node X of coordinates x of the FE mesh the distance to the boundary Γ. In turn, the interface Γ is given by the level 0 of the function ϕ:

$$\begin{cases} \phi(x) = \pm d(x, \Gamma), x \in \Omega \\ \Gamma = \{x \in \Omega, \phi(x) = 0\} \end{cases} \tag{1}$$

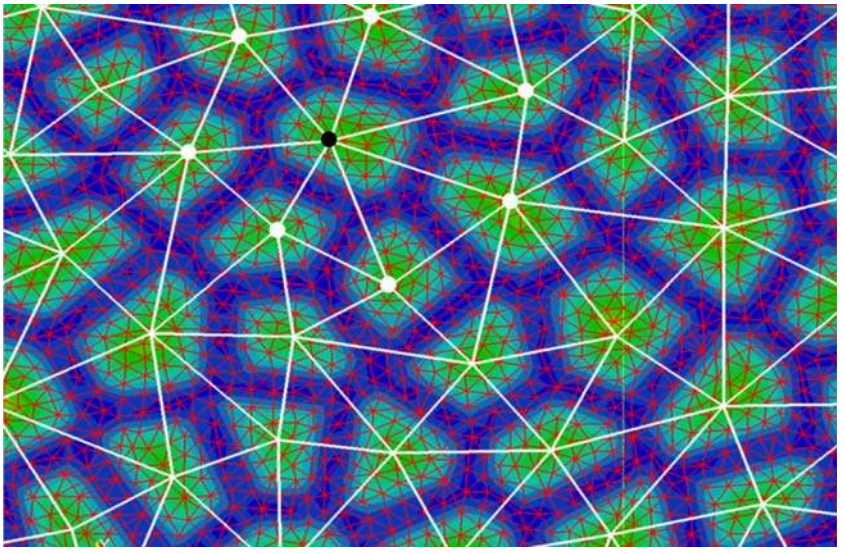

Figure 1. FE mesh (red), Delaunay triangulation (white), the nucleus Si (black), its graph (white points) and the global level-set function defining the Voronoï tessellation. (Available in colour online)

Let us assume that the domain Ω contains N_C cells, we have $\{\phi_i, 1 \leq i \leq N_C\}$ with the sign convention $\phi_i \geq 0$ inside the cell C_i, and $\phi_i \leq 0$ outside. The procedure to evaluate these functions at all nodes X of the FE mesh goes through evaluating the functions:

$$\alpha_{ij}(x) = \frac{1}{2} \parallel \overrightarrow{S_iS_j} \parallel - \frac{\overrightarrow{S_iS_j}.\overrightarrow{S_iX}}{\parallel \overrightarrow{S_iS_j} \parallel} \quad \text{for} \quad 1 \leqslant i,j \leqslant N_C, \quad j \neq i, \tag{2}$$

which correspond to the signed distance of x to the perpendicular bisector of the segment $[S_i, S_j]$, $\phi(x)$ is then defined as:

$$\phi_i(x) = \min_{j \in Graph(S_i)} (\alpha_{ij}(x)), \tag{3}$$

where $Graph(S_i)$ is the graph of the nucleus S_i, which is the set of its neighbours in the Delaunay triangulation (i.e. the nuclei sharing with it an edge of the Delaunay triangulation). A global distance function can also be defined as:

$$\phi_{glob}(x) = \max\{\phi_i(x), 1 \leq j \leq N_C\} \tag{4}$$

This function is positive everywhere and tends to zero on the cell boundary network.

By using the VTM, the nuclei are randomly placed in the computational domain. Thus, equiaxial Voronoï cells with a specific size distribution law cannot be generated. To obtain such microstructures, a distribution of spherical particles that serves as a basis for constructing the microstructure is used. This leads to the use of the LTM (Imai et al., 1985), which consists of assigning a radius, or weight, to each nucleus with no intersections between the created spherical particles, building the corresponding weighted Delaunay triangulation (Glickenstein, 2007) and then constructing its dual, the Laguerre tessellation.

Level-set functions are also used to define the Laguerre cells. These functions are also given by Equation (3), where the $Graph(S_i)$ is then obtained by the weighted Delaunay triangulation and where the functions $\alpha_{ij}(x)$, defined in Equation (2), are modified as follows:

$$\alpha_{ij}(x) = \frac{1}{2}\left(\| \overrightarrow{S_iS_j} \| + \frac{r_i^2 - r_j^2}{\| \overrightarrow{S_iS_j} \|} \right) - \frac{\overrightarrow{S_iS_j}.\overrightarrow{S_iX}}{\| \overrightarrow{S_iS_j} \|} \quad \text{for} \quad 1 \leq i,j \leq N_C, \quad j \neq i, \tag{5}$$

where r_i and r_j are, respectively, the radii of S_i and S_j .

Furthermore, it is important to underline that the principal difficulty of the LTM is common to the packing of polydispersed spheres, to respect a given statistical size of spheres with the highest density possible. If this criterion seems natural for sphere packing, it is also crucial for the LTM in order to limit the heterogeneities between the weight imposed and the size of Laguerre cells finally obtained. For this reason, an advancing front method (Benabbou, Borouchaki, Laug, & Jian, 2009, 2010) is used for the sphere packing in order to respect a given statistical data for the cells' size (Hitti, Laure, Coupez, Silva, & Bernacki, 2012).

2.1. Foams

Boundaries between adjacent cells can be spread by shifting them in the direction of each centre with given values. These values, referred to as ϵ_i, can either follow a specific probability law or be defined by a set of boundary shifts $\{1, \ldots Nc\}$. The new level-set functions are then written as:

$$\phi_i(x) = \min_{j \in Graph(S_i)} (\alpha_{ij}(x)) - \epsilon_i, \tag{6}$$

This cell spreading technique is used to define the thickness of the solid skeleton of polymer foams.

The RVEs of foams have two important parameters, their relative density and their regularity. The relative density of a foam is defined as the solid fraction's surface (volume in 3D) on the computing domain's surface (volume in 3D). In the case of honeycombs, this density is calculated in function of the solid skeleton's thickness. In three-dimensional foams, we add the surface of the cells' faces (if it is a closed-cell). In our method, the relative density is controlled using the cells spreading technique. We first consider the following initial approximative calculation of the current relative density ρ^0:

$$\rho^0 \simeq \frac{\sum_{i=1}^{N_c} F_i \epsilon_i}{|\Omega|}, \tag{7}$$

with F_i which represents the newly formed interfacial area of grain C_i and $|\Omega|$ the domain's volume. In order to obtain a desired relative density ρ^d, all ϵ_i are shifted by a value b. Hence, ρ^d is approximatively equal to:

$$\rho^d \simeq \frac{\sum_{i=1}^{N_c} F_i (\epsilon_i + b)}{|\Omega|}. \tag{8}$$

Finally, the microstructure can be adjusted using:

$$b = \frac{(\rho^d - \rho^0)|\Omega|}{\sum_{i=1}^{N_c} F_i}, \tag{9}$$

and setting:

$$\widetilde{\phi}_i(x) = \phi_i(x) - b, \forall i \in \{1, \ldots, N_c\}. \tag{10}$$

Concerning the regularity, a regular honeycomb (foam in 3D) is composed of identical hexagonal (tetrakaidecahedral in 3D) cells. In order to fit n hexagonal (tetrakaidecahedral) cells into an area (volume) a_0, the distance d_0 between any two adjacent nuclei must be equal to $\sqrt{\frac{2a_0}{n\sqrt{3}}}$ $\left(\frac{\sqrt{6}}{2}(\frac{a_0}{\sqrt{2}n})^{\frac{1}{3}}\right.$ in 3D$\left.\right)$. This is performed by placing the spherical particles, used as a basis for constructing the Laguerre cells, in an hexagonal lattice (body-centred cubic in 3D). To construct a random Voronoï honeycomb (foam) with n cells in the area a_0, and hence to randomly place n discs (spheres) in the area a_0, then the minimum exclusion distance, Δ, between the nuclei must be less than d_0. The value of d_0 is therefore an upper limit on the diameter of the n discs (spheres) which may be accommodated. In order to quantify the regularity of the Voronoï honeycomb (foam), a parameter α is defined as $\frac{\delta}{d_0}$ (Zhu et al., 2006; Zhu & Windle, 2002). Then, $\alpha = 1$ (i.e. $d = d_0$) for a regular hexagonal honeycomb (tetrakaidecahedral foam). For a fully random structure, $\alpha = 0$ $(d = 0)$. By imposing a maximal and minimal radii equal to $d_0/2$ and $\delta/2$, respectively, our LTM, combined with the cell spreading technique, can be used to generate honeycombs and foams with different degrees of regularity (see Figures 2 and 3).

In these figures, the solid skeleton thickness was chosen as a constant all over the domain. But, this thickness can also be heterogeneous by choosing ϵ_i according to specific probability law.

2.2. *Statistical modelling*

In order to show our method's capability of respecting statistical data, a pixelated image of a stainless steel 304L containing 1387 equiaxed cells, obtained by electron backscattered diffraction (EBSD), was used to calculate the cell surface distribution. A part of this image is illustrated in Figure 4 where the grain joints were identified and drawn in white lines. In this figure, the twin boundaries were not taken into account.

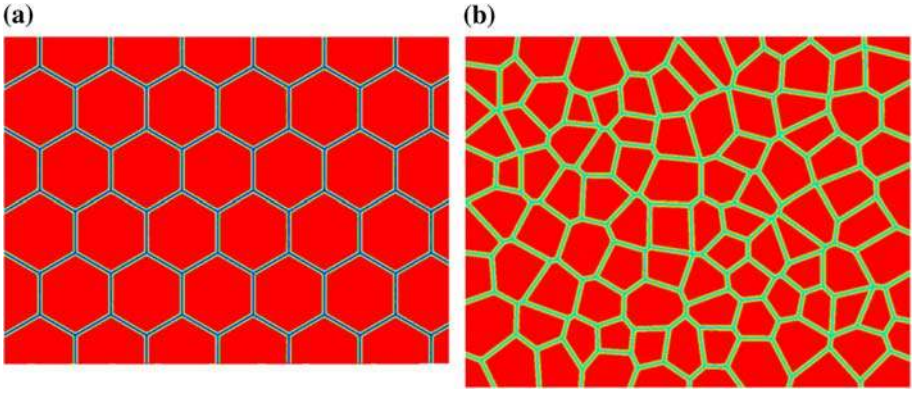

Figure 2. (a) A regular Voronoï honeycomb with relative density of .075 and (b) a honeycomb with a regularity degree of .5 and a relative density of .125.

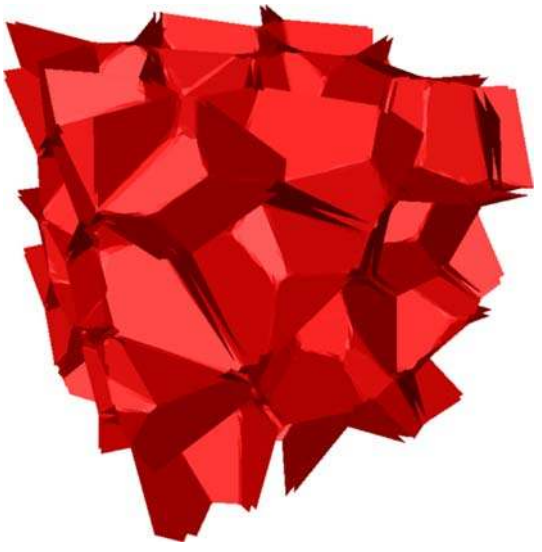

Figure 3. A three-dimensional closed-cell foam with a regularity degree of .5 and a relative density of .2.

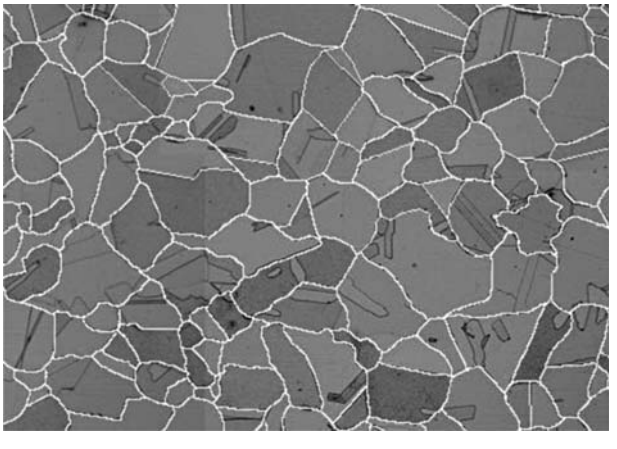

Figure 4. A microscopic illustration of a stainless steel 304L with grain joints drawn in white lines.

Table 1. Statistics (mean for 20 calculations) of the 2D experimental cell case.

Domain	Mean number of grains	L_2 error in %
S_0	38	12.16
S_1	200	4.22
S_2	456	2.97
S_3	875	3.22
S_4	1360	2.17
S_5	2012	2.14

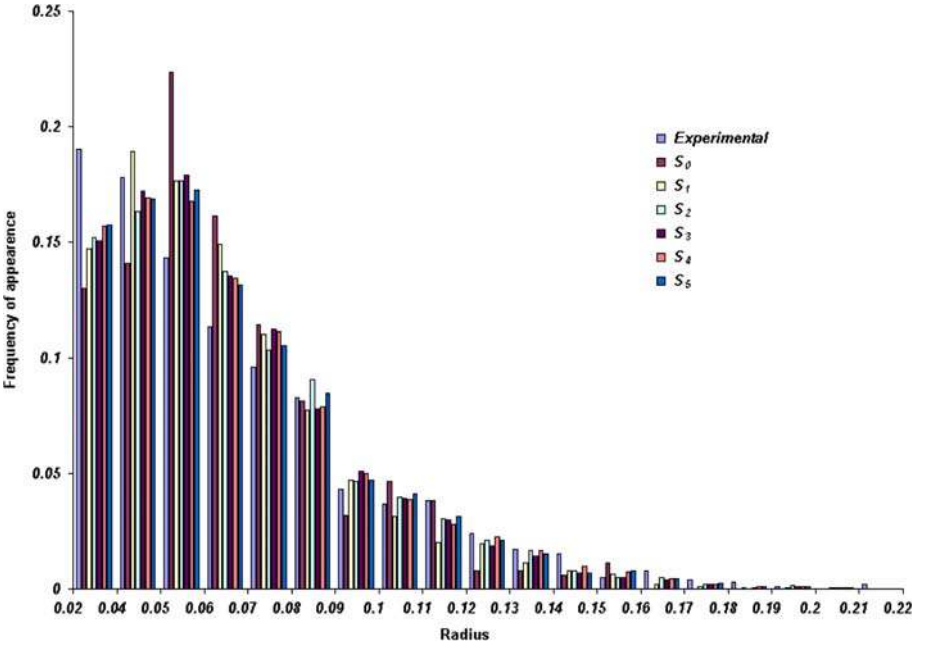

Figure 5. The frequencies obtained in all the domains compared with the experimental frequencies. (Available in colour online)

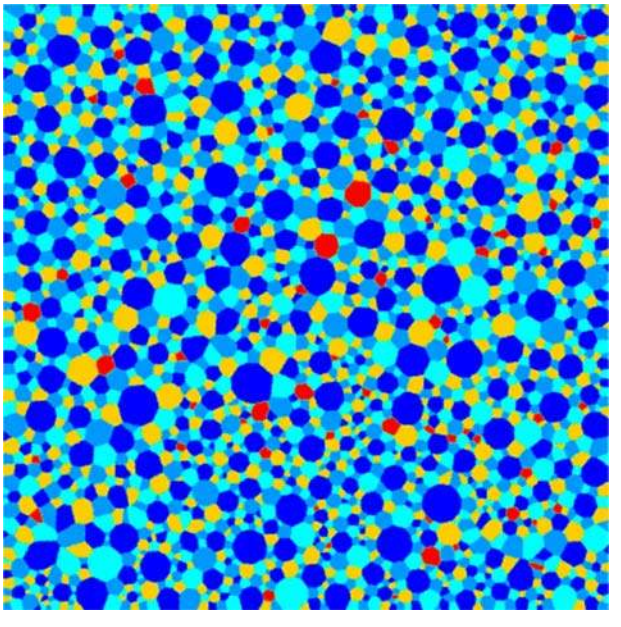

Figure 6. 2237 cells obtained using the LTM method in S_5.

Afterwards, the surface of each grain is calculated using the software Visilog 6.3. This surface is considered as the one of the equivalent generating discs and hence, a statistic of the

equivalent radius is obtained and used for generating the virtual, statistically equivalent, microstructure. The statistic of the equivalent radii was approached by a histogram distribution law. In order to study the evolution of the L_2 error (between the given distribution law and the ones obtained) as a function of the number of particles, the cells were generated for several domains with different sizes. We performed our calculations in six different non-dimensional domains, denoted by $\{S_i, 0 \leq i \leq 5\}$, which correspond, respectively, to a 1×1, 2×2, 3×3, 4×4, 5×5, and 6×6 square domain using the LTM. To be more statistically representative, 20 random configurations were generated for each domain and the data were collected for analysis. The results obtained are summarised in Table 1 and in Figure 5.

The results obtained are very satisfying as we converge towards the exact experimental statistics as the number of grains increases which proves the capability of our methods to respect statistical data. One of the calculations performed in S_5 containing 2237 cells is illustrated in Figure 6.

3. Anisotropic mesh adaptation

As it was mentioned in the introduction, mesh adaptation is necessary to define the RVEs using a level-set framework not only to describe properly the considered microstructure but also to take into account discontinuities of physical properties. Isotropic refinement of the mesh can be used to reach a desired accuracy in the interface description. However, this strategy leads to a significant increase of computation resources. An adaptive anisotropic remeshing technique is therefore preferred. Different ways exist to generate adapted anisotropic meshes. A common approach consists of using an a posteriori error analysis in order to obtain an optimal mesh for a given number of elements (Almeida, Feijoo, Galeao, Padra, & Silva, 2000; Mesri, Zerguine, Digonnet, Silva, & Coupez, 2008). However, this approach could be inappropriate in our case when an important number of level-set functions must be considered. More precisely, when some strictly disjoint objects are described by level-set functions, a simple solution consists to adapt the mesh, thanks to an *a posteriori* error estimator to the corresponding ϕ_{glob} function. However, such an approach is not straightforward when the different objects considered are not strictly disjoint or very close as for the microstructure considered in this work. These remarks explain why we preferred to deal with an automatic geometrical method for the generation of anisotropic mesh. The following method was initially developed for the multiscale modelling of microstructure evolutions in polycrystalline materials (Bernacki, Chastel, Coupez, & Logé, 2008; Bernacki et al., 2009; Bernacki, Logé, & Coupez, 2011; Resk, Delannay, Bernacki, Coupez, & Logé, 2009) and most recently adapted to the generation of granular semi-solid RVEs (Sun, Logé, & Bernacki, 2010). A brief recall of this method is described, and an optimisation procedure is proposed.

The idea of this method consists of fixing mesh refinement in a narrow zone surrounding the different interfaces. Besides, the refinement operates only in the direction perpendicular to the interface, which leads to anisotropic meshes. This anisotropic (re-)meshing method leads to a very high accuracy near the interfaces without increasing dramatically the computation resources (Coupez, Digonnet, & Ducloux, 2000).

The generation of such meshes requires the definition of a metric field and the use of a topological mesher. Anisotropic meshes are built using the MTC mesher–remesher developed by Coupez et al. (2000). It is based on local mesh topology optimisations and works for all meshing applications from adaptive remeshing to mesh generation by using a minimal volume principle. The MTC improves the mesh topology by considering the quality of the elements. The quality of an element is defined through a shape factor which takes into account the

considered metric (Gruau, 2004). A metric is a symmetric positive definite tensor which represents a local base modifying the way to compute a distance, such that:

$$||\vec{u}||_{\mathbf{M}} = \sqrt{{}^t\vec{u}\mathbf{M}\vec{u}}, \quad \langle \vec{u}, \vec{v} \rangle_{\mathbf{M}} = {}^t\vec{u}\mathbf{M}\vec{v}. \tag{11}$$

If $\mathbf{M}$ is the identity tensor, the distance corresponds to the usual one in the Euclidean space. As $\mathbf{M}$ is a symmetric positive definite tensor, it is diagonalisable in an orthonormal basis of eigenvectors, and all the eigenvalues are strictly positive. The metric $\mathbf{M}$ can be interpreted as a tensor whose eigenvalues are linked to the mesh sizes, and eigenvectors defining the directions in which these mesh sizes are applied. Let us consider the simple case of only one interface. The iso-zero of the level set function represents the boundary, Γ, and the gradient of the level-set function defines the normal to the boundary which corresponds to the direction of mesh refinement. To define the mesh size in that direction, and its distribution in space, a characteristic thickness E is introduced:

$$\begin{cases} |\phi(x)| \geq \frac{E}{2} & \text{near the interface} \\ |\phi(x)| > \frac{E}{2} & \text{far from the interface} \end{cases} \tag{12}$$

The mesh size takes a default value far from the interface, and is reduced in the direction perpendicular to the interface when $|\phi(x)|$ is reduced. Let h_2 be the desired refined mesh size in the direction of $\nabla\phi$, and h_1 the desired mesh size in the directions perpendicular to $\nabla\phi$. Let us finally require an isotropic mesh size equal to h_0 outside the anisotropic boundary layer. The corresponding metric $\mathbf{M}$ is then expressed as follows:

$$\mathbf{M} = C(\nabla\phi \otimes \nabla\phi) + B\mathbf{I}, \tag{13}$$

with $\mathbf{I}$ the identity matrix, B and C scalars given by:

$$B = \begin{cases} \frac{1}{h_0^2} & if \quad |\phi(x)| > \frac{E}{2} \\ \frac{1}{h_1^2} & if \quad |\phi(x)| \leq \frac{E}{2} \end{cases}, \quad C = \begin{cases} 0 & if \quad |\phi(x)| > \frac{E}{2} \\ \frac{1}{h_2^2} - \frac{1}{h_1^2} & if \quad |\phi(x)| \leq \frac{E}{2} \end{cases} \tag{14}$$

The eigenvalues of the metric near the boundary are $\lambda_2 = (1/h_2^2 - 1/h_1^2)||\nabla\phi|| + 1/h_1^2 = 1/h_2^2$, and $\lambda_1 = \lambda_3 = 1/h_1^2$. The former is associated to the eigenvector $v_2 = \nabla\phi$, and the latter to the basis vectors $(\mathrm{v}_1, \mathrm{v}_3)$ of the plane tangent to the boundary. Clearly, if h_2 is chosen much smaller than h_1, which is chosen equal to h_0, $\nabla\phi$ corresponds to the refinement direction and the elements are stretched in the tangent plane.

It could be also underlined that working with less (respectively more) anisotropic mesh near the interface corresponds to taking a value of h_2 less close (respectively closer) to h_1. Furthermore, defining h_2 as a function of ϕ and not as a constant enables to obtain a progressive anisotropic refinement rather than a rough anisotropic refinement. When dealing with strictly separated cells (for example, solid grains in a semi-solid granular structure in Sun et al. (2010)), the above technique can be used by considering the global following distance function $\phi_{glob}(x)$. However, when contact exists or when the cells are very close (as for a foam with a very low relative density), this technique can no longer be used. Indeed, the gradient of the function $\phi_{glob}(x)$ then becomes extremely large and the normal to the interfaces is not properly defined. To solve this difficulty, multiple level set functions are used (one for each cell) to characterise the appropriate refinement directions and the corresponding metric. Two cases can be considered:

(A) $|\phi_i(x)| > \frac{E}{2}$ for $1 \leq i \leq N_c$, which means that x lies far from any cell interface. These points correspond to the isotropic regions with mesh size h_0 .

(B) $|\phi_i(x)| \leq \frac{E}{2}$ for n cells, $n \leq N_c$. The n vectors $\nabla\phi_i$ along which refinement is required define a vector space $\boldsymbol{V}$ of dimension 1, 2 or 3.

In case (B), if $\boldsymbol{V}$ is one-dimensional, there is only one direction of mesh refinement and the metric takes the form given by Equations (13) and (14). When $\boldsymbol{V}$ is three-dimensional, an isotropic metric is chosen, this time with the reduced mesh size h_2. When $\boldsymbol{V}$ is two-dimensional, the required refinement is obtained with the following metric:

$$\mathbf{M} = C(\nabla\phi_1 \otimes \nabla\varphi_1) + C(\overrightarrow{w} \otimes \overrightarrow{w}) + BI, \tag{15}$$

with $\overrightarrow{w}$ such as $(\nabla\phi_1, \vec{w})$ corresponds to an orthonormal basis of $\boldsymbol{V}$. The metric given by Equation (15) prescribes, in the anisotropic zone, a mesh size h_2 in the plane $\boldsymbol{V}$, and a mesh size h_1 in the direction normal to $\boldsymbol{V}$ (which implies an isotropic mesh of mesh size equal to near the interface in 2D context). Figure 7 illustrates a result obtained for a Voronoï honeycomb in a unit square made of 74 Laguerre cells. The anisotropic mesh adaptation was realised at the cells interfaces with the following parameters: $h_1 = h_0 = .01$ and $h_2 = 10^{-4}$. The anisotropic mesh, made of 91,764 nodes and 181,867 elements, was obtained in four minutes in an eight processors parallel calculation. The zoom in Figure 7(b) illustrates the good meshing adaptation obtained at a triple junction with fine isotropic elements as required by the number of independent refinement directions.

If this approach is efficient and allows obtaining easily appropriate meshing adaptation for complex RVEs, its principal weakness remains its numerical cost particularly in 3D. A first waste of computational resources can be identified in the fact to work with one level-set per cell. Indeed, on the majority of the RVEs considered, the microstructure is built to represent only two phases as for granular semi-solid or foam obtained by spreading Voronoï tessellation. Even for the recrystallisation modelling in polycrystal RVEs, a global velocity depending of local characteristics can be defined without the knowledge of individual grains (Bernacki et al., 2008, 2009). Finally, in all these cases, knowing the individual level-set function of each

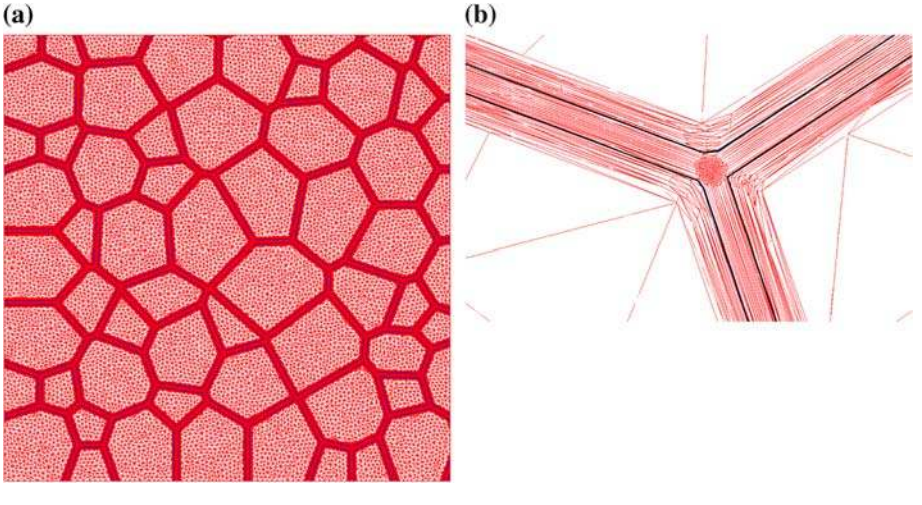

Figure 7. (a) Anisotropic meshing adaptation for a Voronoï honeycomb and (b) zoom at a triple junction. The iso-zero of the level-set function defining the honeycomb is shown in black.

cell is not a necessity to perform numerical modelling. Moreover, the important point for the meshing strategy proposed is not inevitable to know all the level-set functions but to deal with a set of level-set functions representing sets of strictly disjoints cells and which the gathering corresponds to the whole microstructure considered. The simple method proposed here, to limit the number of requisite level-set functions for meshing adaptation, is to use the classical technique of graph colouration (Kubale, 2004). The idea is to colour the vertices of a graph such that no two adjacent vertices share the same colour with a minimal number of colours. Graph colouring is a very active field of research and some results of this domain are famous such as the four colour theorem (Appel & Haken, 1976). The idea developed in this work is to use a simple graph colouring algorithm of the Delaunay triangulation calculated in our algorithm of generation of RVEs to gather all the level-set functions of the cells involved in few new level-set functions presenting the properties to correspond to a set of strictly disjointed cells and so, usable for the meshing strategy described previously.

Although quite old, the DSATUR colouration algorithm (Brélaz, 1979) remains an interesting choice of colouring method in term of ratio "computational cost/number of colours obtained". This algorithm was added to our RVE builder and some examples are given below. A comparison of computational costs was done on a Voronoï honeycomb made of 356 cells. When the DSATUR algorithm was used, five level-set functions were used to construct an anisotropic mesh made of 302,110 nodes and 602,505 elements in 16 minutes and 43 seconds using 8 processors. When the DSATUR algorithm was not used, 356 level-set functions were used (one level-set for each grain) to construct an anisotropic mesh made of 306,501 nodes and 611,298 elements in 1 hour 3 minutes and 40 seconds using the same number of processors. Two figures illustrate the efficiency of our algorithm. The case of Figure 8(a) corresponds to a Voronoï honeycomb made of 813 cells with a relative density of .04, and represented using five level-set functions obtained with the DSATUR algorithm (one colour per level-set function). The zoom in Figure 8(b) illustrates the anisotropic meshing adaptation obtained, thanks to the metric defined by Equations (14) and (15) and calculated with the five level-set functions. The mesh is made of 530,071 nodes and 1,056,388 elements and was generated in 47 min using eight processors. Figure 9 illustrates a three-dimensional tetrakaidecahedral closed-cell foam made of 250 cells with a relative density of .2, generated using

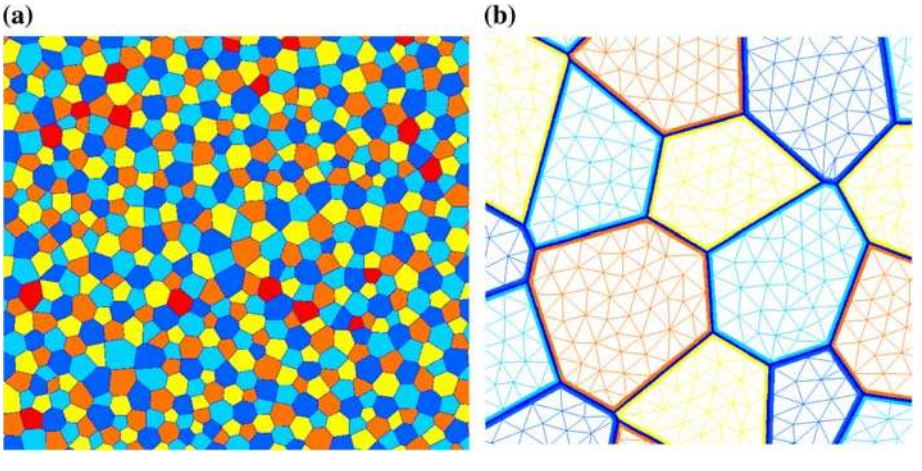

Figure 8. (a) A Voronoï honeycomb made of 813 Laguerre cells with a relative density of .04, described using five level-set functions and (b) a zoom illustrating anisotropic meshing at the interfaces of the Laguerre cells.

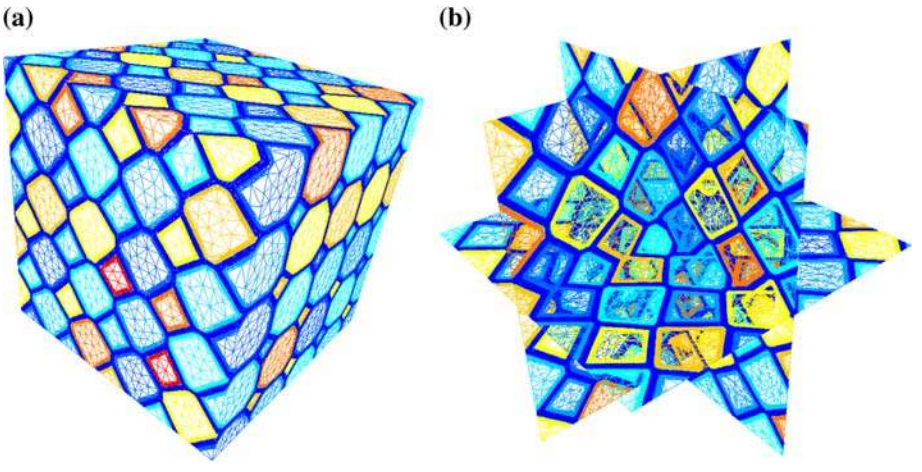

Figure 9. (a) A 3D tetrakaidecahedral foam microstructure made of 250 cells with a relative density of .2, generated using the LTM and described by eight level-set functions and (b) mesh on three orthogonal cross sections.

the LTM and represented by eight level-set functions. The anisotropic mesh in this case is made of 768,326 nodes and 4,331,151 elements.

4. Foam compression

Before detailing the simulations performed, we will explain the governing equations and the FE formulation of our FSI problem.

4.1. Governing equations

The mechanical problem is governed by the momentum equation, in which gravity and inertia effects are neglected, and by the continuity equation:

$$\nabla \cdot \sigma = 0, \tag{16}$$

$$\frac{\partial \rho}{\partial t} + \nabla \cdot (\rho \mathbf{v}) = 0, \tag{17}$$

where σ is the stress tensor, ρ is the density and $\mathbf{v}$ is the velocity.

The aforementioned partial differential equations are valid for both solids and fluids. The difference lies in the constitutive relation for the stress tensor. In fluids, it is expressed in terms of the strain rate tensor (i.e. velocities) and pressure, while in solids, it is a function of the strain tensor (i.e. displacements). More specifically, for a linear, viscous (or Newtonian) fluid, the stress tensor σ_f is given by:

$$\sigma_f = 2\eta_f \epsilon(\mathbf{v}) - \left(\frac{2}{3}\eta_f \nabla \cdot \mathbf{v} + p\right) I, \tag{18}$$

where η_f is the laminar viscosity of the fluid, p is the pressure, I is the identity matrix and $\epsilon(\mathbf{v})$ is the strain rate tensor which is defined by:

$$\epsilon(\mathbf{v}) = \frac{1}{2}(\nabla\mathbf{v} + \nabla\mathbf{v}^T), \tag{19}$$

where $\nabla\mathbf{v}^T$ is the transpose of the velocity's gradient $\nabla\mathbf{v}$. For an incompressible flow, which is not the case in this application because the air is a weakly compressible fluid, $\nabla.\mathbf{v} = 0$, and the second term on the right-hand side of Equation (18) will contain only the pressure. By writing Equation (18) with a modified pressure $p' = p + \frac{2}{3}\eta_f \nabla\mathbf{v}$ and replacing σ_f in Equation (16), we get:

$$2\eta_f \nabla \cdot (\epsilon(\mathbf{v})) - \nabla p' = 0. \tag{20}$$

For a linear, elastic solid, the stress tensor σ_s is given by the generalised Hooke's law:

$$\sigma_s = 2\mu\epsilon(\mathbf{u}) + \lambda tr\epsilon(\mathbf{u})I, \tag{21}$$

where μ and λ are the two Lamé coefficients, $\mathbf{u}$ is the displacement, $\epsilon(\mathbf{u})$ is the strain tensor and $tr(.)$ is the trace operator where $tr(\epsilon(\mathbf{u})) = \nabla.\mathbf{u}$. The Lamé coefficients are related to the Young's modulus (E) and the Poisson ratio (v) by the following expressions:

$$\begin{aligned} \lambda &= \tfrac{vE}{(1+v)(1-2v)}, \\ \mu &= \tfrac{E}{2(1+v)}. \end{aligned} \tag{22}$$

Equation (21) is not general as it cannot be used for incompressible solids for which $v = .5$. The reason is that the Lamé coefficient λ tends to infinity and $tr\epsilon(\mathbf{u})$ is null so their product is indeterminable. Although, the foam's solid skeleton is compressible, writing a general form of this equation is preferred. Hence, the pressure is treated as a separate unknown variable. In solid mechanics, the pressure is defined as:

$$p = -\frac{\sigma_s}{3}, \tag{23}$$

and the bulk modulus K is related to the Lamé coefficients by:

$$K = \frac{2}{3}\mu + \lambda. \tag{24}$$

Using the two previous relations, we can easily show that the pressure can be written as:

$$p = -Ktr(\epsilon(\mathbf{u})). \tag{25}$$

Moreover, the bulk modulus is defined by,

$$K = -V\frac{\partial p}{\partial V}, \tag{26}$$

where V is the fluid's volume. Using Equations (24) and (25), the following relation can be written as:

$$\lambda \cdot tr(\epsilon(\mathbf{u})) = -\left(p + \frac{2}{3}\mu tr(\epsilon(\mathbf{u}))\right). \tag{27}$$

This relation is used in Equation (21) which introduces the pressure to the solid's constitutive equation:

$$\sigma_s = 2\mu\epsilon(\mathbf{u}) - \left(\frac{2}{3}\mu tr(\epsilon(\mathbf{u})) + p\right)I. \tag{28}$$

By writing Equation (28) with a modified pressure $p' = p + \frac{2}{3}\mu\nabla\cdot\mathbf{u}$ and replacing σ_s in Equation (16), we get:

$$2\mu\nabla\cdot(\epsilon(\mathbf{u})) - \nabla p' = 0. \tag{29}$$

The additional unknown (pressure) is obtained by rearranging Equation (25):

$$\nabla\cdot\mathbf{u} + \frac{1}{K}p = 0. \tag{30}$$

Equation (29) is supplemented by Equation (30) as well as the relationship between displacements and solid velocities and hence, a system of equations is obtained for the solid:

$$\begin{cases} 2\mu\nabla\cdot(\epsilon(\mathbf{u})) - \nabla p' = 0 \quad \text{(a)} \\ \frac{d\mathbf{u}}{dt} = \mathbf{v} \quad \text{(b)} \\ \nabla\cdot\mathbf{u} + \frac{1}{K}(p' - \frac{2}{3}\mu\nabla\cdot\mathbf{u}) = 0 \quad \text{(c)} \end{cases} \tag{31}$$

The corresponding system for a weakly compressible fluid is:

$$\begin{cases} 2\eta_f\nabla\cdot(\epsilon(\mathbf{v})) - \nabla p' = 0 \quad \text{(a)} \\ \nabla\cdot\mathbf{v} + \frac{1}{K}\frac{dp'}{dt} = 0 \quad \text{(b)} \end{cases} \tag{32}$$

where the definition of the bulk modulus of the fluid K (i.e. Equation (26)) was used in Equation (17) in order to write the second equation of the fluid's system.

Also, by using the definition of the bulk modulus K, and the fact that the air is an ideal gas which mean PV is a constant in isothermal conditions, Equation (32(b)) can be written as:

$$\nabla\cdot\mathbf{v} + \frac{1}{p'}\frac{dp'}{dt} = 0. \tag{33}$$

A velocity–pressure formulation should be written for the solid in order to solve a coupled FSI problem. The displacement is linked to the velocity by Equation (31(b)) and since a Lagrangian framework is used, this equation could be written as:

$$\mathbf{u}^t = \mathbf{u}^{t-\Delta t} + \mathbf{v}^t\Delta t. \tag{34}$$

Using this expression for the displacement in the solid's system of Equations (31), this system could be written as:

$$\begin{cases} 2\mu\Delta t\nabla\cdot(\epsilon(\mathbf{v}^t)) - \nabla p'^t = -2\mu\nabla\cdot(\epsilon(\mathbf{u}^{t-\Delta t})) \quad \text{(a)} \\ \nabla\cdot\mathbf{v}^t + \frac{1}{K-\frac{2}{3}\mu}\frac{dp'^t}{dt} = 0 \quad \text{(b)} \end{cases} \tag{35}$$

The expression $-2\mu\epsilon(\mathbf{u}^{t-\Delta t})$ of the right-hand side of Equation (35(a)) is the extra-stress tensor in the governing Stokes equations. Equation (35(b)) is obtained by rearranging Equation (31(c)) to the form:

$$\nabla \cdot \mathbf{u} = -\frac{1}{K - \frac{2}{3}\mu} p'. \tag{36}$$

Then, replacing $\nabla \cdot \mathbf{u}^t$ and $\nabla \cdot \mathbf{u}^{t-\Delta t}$ by their suitable expression in:

$$\nabla \cdot \mathbf{u}^t = \nabla \cdot \mathbf{u}^{t-\Delta t} + \nabla \cdot \mathbf{v}^t \Delta t. \tag{37}$$

Moreover, using the expression of the bulk modulus K in Equation (24), Equation (35(b)) could be written as:

$$\nabla \cdot \mathbf{v}^t + \frac{1}{\lambda} \frac{dp'^t}{dt} = 0. \tag{38}$$

Finally, the governing equations for the FSI problem are defined by Equation (39) for the fluid and Equation (40) for the solid:

$$\begin{cases} 2\eta_f \nabla \cdot (\epsilon(\mathbf{v}^t)) - \nabla p'^t = 0 \\ \nabla \cdot \mathbf{v}^t + \frac{1}{p'^t} \frac{dp'^t}{dt} = 0 \end{cases} \tag{39}$$

$$\begin{cases} 2\mu\Delta t \nabla \cdot (\epsilon(\mathbf{v}^t)) - \nabla p'^t = -2\mu \nabla \cdot (\epsilon(\mathbf{u}^{t-\Delta t})) \\ \nabla \cdot \mathbf{v}^t + \frac{1}{\lambda} \frac{dp'^t}{dt} = 0 \end{cases} \tag{40}$$

4.2. Numerical approach

Since we have two phases, solid and fluid, the computational domain Ω is decomposed into two subdomains, Ω_s and Ω_f, designating, respectively, the solid domain and the fluid domain which is described by the level-set function ϕ_{glob} (see Equation (4)). The location of the solid is then deduced by complementarity and does not require the introduction of an additional distance function. Once calculated, the level-set allows us to define a presence function of the subdomain Ω_i. A smoothed Heaviside function $H(\phi_{glob})$ is used in this work, where a thickness e is fixed near the interface in order to prevent a discontinuous transition in this region. The value of e is chosen accordingly to the mesh size. The function $H(\phi_{glob})$ is defined as:

$$H(\phi_{glob}) = \begin{cases} 0 & \text{if} \quad \phi_{glob} < -e \\ \frac{1}{2}\left(1 + \frac{\phi_{glob}}{2}\right) & \text{if} \quad |\phi_{glob}| \leq e \\ 1 & \text{if} \quad \phi_{glob} > e \end{cases} \tag{41}$$

Furthermore, the objective being to calculate the physical properties on the entire geometry Ω, mixing laws (Hachem, Kloczko, Digonnet, & Coupez, 2012) are introduced and anisotropic adaptive meshing is used. These laws are defined as functions of the

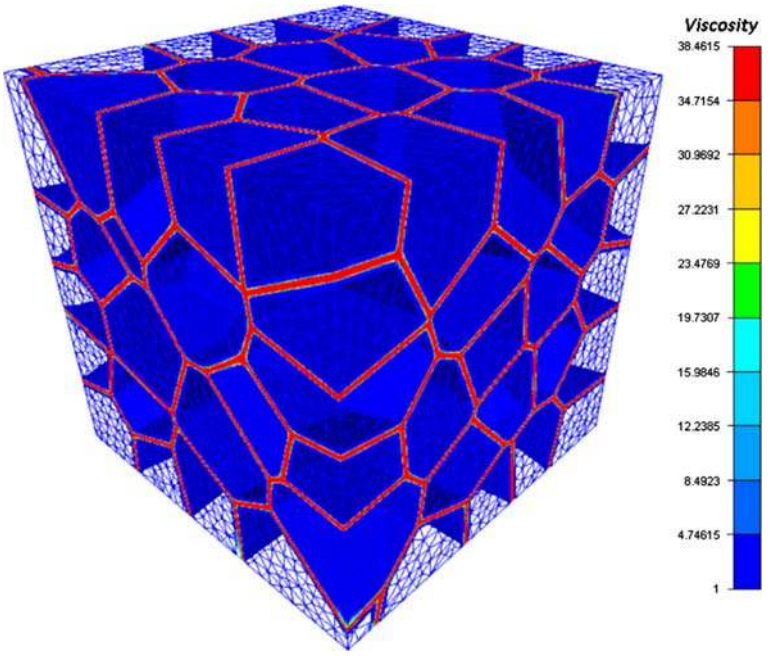

Figure 10. Mixing the air's viscosity η_f with $\mu\Delta t$. The surface mesh is shown in blue. (Available in colour online)

level-set. For all variables Θ, such as the viscosity and the compressibility coefficient, a linear mixing rule is applied at the neighbourhood of the interface between two subdomains Ω_s and Ω_f:

$$\Theta = H(\phi_{glob})\Theta_f + (1 - H(\phi_{glob}))\Theta_s. \tag{42}$$

We used the mixing rules to mix the viscosities and the compressibility coefficients of the solid and fluid (see Figure 10) by writing:

$$\Psi = H(\phi_{glob})\eta_f + (1 - H(\phi_{glob}))\mu\Delta t, \tag{43}$$

and

$$\chi = H(\phi_{glob})\frac{1}{p'} + (1 - H(\phi_{glob}))\frac{1}{\lambda}, \tag{44}$$

which gives us the final system of our FSI problem where, for the sake of clarity, p'^t is denoted as p and $\mathbf{v}^t$ is denoted as $\mathbf{v}$:

$$\begin{cases} 2\Psi\nabla\cdot(\epsilon(\mathbf{v})) - \nabla p = -2\mu\nabla\cdot(\epsilon(\mathbf{u}^{t-\Delta t})) \\ \nabla\cdot\mathbf{v} + \chi\frac{dp}{dt} = 0 \end{cases} \tag{45}$$

This system of equations is solved using a mixed FE method that we are going to detail in the next section.

4.3. The FE formulation

First, let us define the function spaces used in the remainder of this paper. The scalar function space for the pressure is $Q = \mathcal{L}^2(\Omega)$, the function spaces for the velocity are $V = (\mathcal{H}^1(\Omega))^d$ and $V_0 = (\mathcal{H}^1_0(\Omega))^d$, where d is the space dimension, $\mathcal{L}^2(\Omega)$ is the Lebesgue space of square assumable functions on Ω and $\mathcal{H}^1(\Omega)$ is the Sobolev space included in $\mathcal{L}^2(\Omega)$:

$$\begin{cases} \mathcal{L}^2(\Omega) = \{q / \int_\Omega q^2 d\Omega < \infty\} \\ \mathcal{H}^1(\Omega) = \{u \in \mathcal{L}^2(\Omega) / \nabla u \in \mathcal{L}^2(\Omega)\} \\ \mathcal{H}^1_0(\Omega) = \{u \in \mathcal{H}^1(\Omega) / u = 0 \text{ on } \partial\Omega\} \end{cases}$$

Moreover, $(.,.)_\Omega$, which denotes the dot product in $\mathcal{L}^2(\Omega)$, is defined as:

$$(u, v)_\Omega = \int_\Omega u(x)v(x)d\Omega. \tag{46}$$

4.3.1. Classical mixed formulation

The FE formulation begins by writing the weak form of the compressible Stokes Equations (45). The problem consists of finding $(\mathbf{v}, p) \in V \times Q$ such that $\forall(\mathbf{w}, q) \in V_0 \times Q$:

$$\begin{cases} 2\Psi(\epsilon(\mathbf{v}):\epsilon(\mathbf{w}))_\Omega - (p, \nabla.\mathbf{w})_\Omega = -2\mu(\epsilon(\mathbf{u}^{t-\Delta t}):\epsilon(\mathbf{w}))_\Omega \\ -(\nabla.\mathbf{v}, q)_\Omega - (\frac{\gamma}{\Delta t} p^t, q)_\Omega = -(\frac{\gamma}{\Delta t} p^{t-\Delta t}, q)_\Omega \end{cases} \tag{47}$$

The Galerkin approximation consists of decomposing our domain Ω into N_{el} simplices T such that they cover the domain and they are either disjoint or share a complete edge. The triangulation will be denoted $\mathcal{T}_h$. Using this partition, the above-defined functional spaces are approached by finite dimensional spaces, used in the remainder of this paper, spanned by continuous piecewise polynomials such that:

$$\begin{cases} Q_h = \{q_h \in C^0(\Omega) / q_{h|T} \in P^1(T), \forall T \in \mathcal{T}_h\} \\ V_h = \{\mathbf{v_h} \in (C^0(\Omega))^d / \mathbf{v_{h|T}} \in (P^1(T))^d, \forall T \in \mathcal{T}_h\} \\ V_{h,0} = \{\mathbf{v_h} \in V_h / \mathbf{v_{h|\Gamma}} = 0\} \end{cases}$$

where $P^1(T)$ is the vector space of first-degree polynomials defined on the simplex T .

The Galerkin discrete problem consists now of solving the mixed problem by finding the pair $(\mathbf{v_h}, p_h) \in V_h \times Q_h$ such that $\forall(\mathbf{w_h}, q_h) \in V_{h,0} \times Q_h$:

$$\begin{cases} 2\Psi(\epsilon(\mathbf{v_h}) : \epsilon(\mathbf{w_h}))_\Omega - (p_h, \nabla \cdot \mathbf{w_h})_\Omega = -2\mu(\epsilon(\mathbf{u}_\mathbf{h}^{t-\Delta t}) : \epsilon(\mathbf{w_h}))_\Omega \\ -(\nabla \cdot \mathbf{v_h}, q_h)_\Omega - (\frac{\gamma}{\Delta t} p_h^t, q_h)_\Omega = -(\frac{\gamma}{\Delta t} p_h^{t-\Delta t}, q_h)_\Omega \end{cases} \tag{48}$$

It is known that the FE approximation (48) may fail because of the inf–sup condition (Brezzi–Babuska) which requires an appropriate pair of function spaces for the velocity and the pressure (Franca, Nesliturk, & Stynes, 1998). In the present work, we aim to retain the advantages of using linear approximations ($P1$ FEs) regarding the accuracy and the computa-

tional cost. But, it is well known that the combination of $P1/P1$ approximation for the velocity and the pressure does not lead to a stable discretisation of system (48) since it fails to satisfy the inf–sup condition:

$$\inf_{q_h \in Q_h} \sup_{\mathbf{v_h} \in V_h} \frac{(\nabla \cdot \mathbf{v_h}, q_h)_\Omega}{\| q_h \|_0 \| v_h \|_1} \geqslant \beta \geqslant 0, \tag{49}$$

where β is a constant independent of h, $\| \, . \, \|_0$ and $\| \, . \, \|_1$ are the norms of $\mathcal{L}^2(\Omega)$ and $\mathcal{H}^1(\Omega)$, respectively.

4.3.2. Stable mixed formulation

A very popular method was proposed by Arnold, Brezzi, & Forti (1984) for the Stokes problem to respect the velocity–pressure compatibility condition. It was suggested to enrich V_h with the space of bubble functions known as mini-element or $P1 + /P1$ (see Figure 11) denoted V^b:

$$V^b = \{v^b / v^b|_{T_i} \in P^1(T_i) \cap H_0^1(T_i), \forall T \in \mathcal{T}_h, i = 1, \ldots, D\}, \tag{50}$$

where D is the topological dimension and T_i is a decomposition of T in D sub-simplices, that have as a common vertex barycenter, G_T, of T. In other words, the choice of this bubble function is continuous inside the element, considered as linear on each sub-simplex and vanishes at the boundary of T .

The velocity field is now an element of the function space generated by the following direct sum:

$$\mathcal{V}_h = V_h \oplus V^b. \tag{51}$$

Hence, on each element T, the solution takes the form:

$$\mathbf{v_h}|_T = \sum_i^D v_T^i N_i + v_T^b b_T, \tag{52}$$

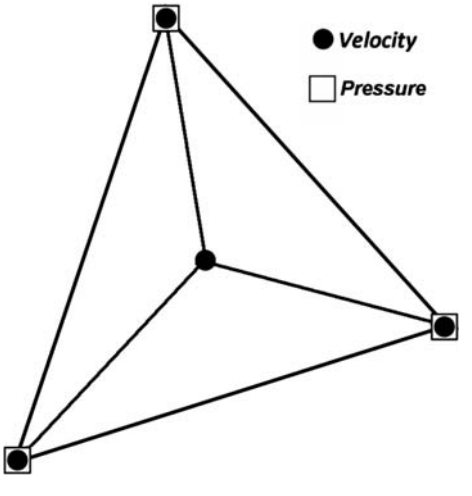

Figure 11. The MINI-element P1 + /P1.

where N_i is the interpolation function associated with node i. The bubble function b_T is defined on each element T as follows: $b_T = 0$ on ∂T ; $b_T(G_T) = 1$. Furthermore, b_T satisfies the orthogonality condition:

$$\int_T \partial_{x_k} N_i \partial_{x_l} b_T d\Omega = 0 \ \forall (k,l,N_i) \in [0,d-1)^2 \times P^1(T). \tag{53}$$

The mixed FE approximation of problem (48) consists now of finding the pair $(\mathbf{v}, p_h) \in \mathcal{V}_h \times \mathcal{Q}_h$ such that $\forall (\mathbf{w}, q_h) \in \mathcal{V}_{h,0} \times \mathcal{Q}_h$:

$$\begin{cases} 2\Psi(\epsilon(\mathbf{v}) : \epsilon(\mathbf{w}))_\Omega - (p_h, \nabla \mathbf{w})_\Omega = -2\mu(\epsilon(\mathbf{u}^{t-\Delta t}) : \epsilon(\mathbf{w}))_\Omega \\ -(\nabla \mathbf{v}, q_h)_\Omega - (\frac{\chi}{\Delta t} p_h^t, q_h)_\Omega = -(\frac{\chi}{\Delta t} p_h^{t-\Delta t}, q_h)_\Omega \end{cases} \tag{54}$$

Since the fine-scale problem is independent and uncoupled at the element level and vanishes on the element boundaries, the system (54) can be decomposed into:

$$\begin{cases} 2\Psi(\epsilon(\mathbf{v_h}) : \epsilon(\mathbf{w_h}))_\Omega - (p_h, \nabla \cdot \mathbf{w_h})_\Omega = -2\mu(\epsilon(\mathbf{u_h}^{t-\Delta t}) : \epsilon(\mathbf{w_h}))_\Omega \\ 2\Psi(\epsilon(\mathbf{v^b}) : \epsilon(\mathbf{w^b}))_\Omega - (p_h, \nabla \cdot \mathbf{w^b})_\Omega = -2\mu(\epsilon(\mathbf{u^{b}}^{t-\Delta t}) : \epsilon(\mathbf{w^b}))_\Omega \\ -(\nabla \cdot \mathbf{v_h}, q_h)_\Omega - (\nabla \cdot \mathbf{v^b}, q_h)_\Omega - (\frac{\chi}{\Delta t} p_h^t, q_h)_\Omega = -(\frac{\chi}{\Delta t} p_h^{t-\Delta t}, q_h)_\Omega \end{cases} \tag{55}$$

As the fine-scale space is assumed to be orthogonal to the FE space, the crossed viscous terms in the equations of (55) vanished (Coupez, 1996).

4.3.3. *Matrix formulation*

The equations of system (55) give rise to the following global system to solve:

$$\begin{pmatrix} A_{ww} & 0 & A_{wq}^t \\ 0 & A_{bb} & A_{bq}^t \\ A_{wq} & A_{bq} & A_{qq} \end{pmatrix} \begin{pmatrix} \mathbf{v_h} \\ \mathbf{v^b} \\ p_h \end{pmatrix} \begin{pmatrix} B_w \\ B_{wb} \\ B_q \end{pmatrix}, \tag{56}$$

where

$$\begin{aligned} &A_{ww}(\mathbf{v_h}) = 2\Psi(\epsilon(\mathbf{v_h}) : \epsilon(\mathbf{w_h}))_\Omega, \quad A_{bb}(\mathbf{v^b}) = 2\Psi(\epsilon(\mathbf{v^b}) : \epsilon(\mathbf{w^b}))_\Omega, \\ &A_{wq}(\mathbf{v_h}) = -(\nabla \cdot \mathbf{v_h}, q_h)_\Omega, \quad A_{bq}(\mathbf{v^b}) = -(\nabla \cdot \mathbf{v^b}, q_h)_\Omega, \\ &A_{wq}^t(p_h) = -(p_h, \nabla \cdot \mathbf{w_h})_\Omega, \quad A_{bq}^t(p_h) = -(p_h, \nabla \cdot \mathbf{w^b})_\Omega, \\ &A_{qq}(p_h) = -(\tfrac{\chi}{\Delta t} p_h, q_h)_\Omega, \quad B_w = -2\mu(\epsilon(\mathbf{u_h}^{t-\Delta t}) : \epsilon(\mathbf{w^b}))_\Omega, \\ &B_{wb} = -2\mu(\epsilon(\mathbf{u^{b}}^{t-\Delta t}) : \epsilon(\mathbf{w_h}))_\Omega, \quad B_q = -(\tfrac{\chi}{\Delta t} p_h^{t-\Delta t}, q_h)_\Omega. \end{aligned} \tag{57}$$

The static condensation process consists of solving the second line for the bubble function v^b and inserting the result into the third line of (56) which yields the condensed matrix scheme for large-scale unknowns $\mathbf{v_h}$ and p_h:

$$\begin{pmatrix} A_{ww} & A_{wq}^{t} \\ A_{wq} & \widetilde{A}_{qq} \end{pmatrix} \begin{pmatrix} \mathbf{v_h} \\ p_h \end{pmatrix} \begin{pmatrix} B_w \\ \widetilde{B}_q \end{pmatrix}, \tag{58}$$

where

$$\begin{aligned} \widetilde{A}_{qq} &= A_{qq} - A_{bq} \cdot A_{bb}^{-1} \cdot A_{bq}^{t}, \\ \widetilde{B}_q &= B_q - A_{bq} \cdot A_{bb}^{-1} \cdot B_{wb}. \end{aligned} \tag{59}$$

It is clear that taking into account locally the influence of fine scales (bubble functions) upon the resolved large scales has introduced new stabilising terms and has modified the components of the global matrix. The new operator $\widetilde{A}_{qq}$ provides a so-called pressure stabilisation while the new right-hand side $\widetilde{B}_q$ ensures consistency (Hachem, 2009).

4.4. *Simulations and discussions*

The solid skeleton was prescribed to be of equal and uniform thickness. This thickness, manipulated using the cell spreading technique (see Section 2.1), controls the foam's relative density, ρ, which was maintained at approximately .1 in these simulations. The Young's modulus of the solid, E, was set to $10^8 Pa$, and its Poisson's ratio was set to .3.

In order to be symmetric, biaxial compression was simulated for all cases by imposing displacements on the domain's upper and lower boundaries. Symmetrical boundary conditions were imposed on the domain's left and right boundaries by writing $\mathbf{v}.\mathbf{n} = 0$, where $\mathbf{n}$ is the outwards pointing vector of each boundary. Depending on the foam's irregularity α, strains ranging from .15 to .3 were achieved using our approach. Furthermore, the following reduced stress (Zhu et al., 2006; Zhu & Windle, 2002) was used:

$$\overline{\sigma} = \frac{\sigma}{E\rho^3}. \tag{60}$$

The stress, in the compression direction, is calculated as the mean of the values on the simplices of an elementary volume. Because the solid material is assumed to be elastic throughout the deformation, the adoption of Equation (60) can eliminate the effect of the foam's relative density and the solid's Young's modulus and make the results more useful.

4.4.1. *The RVE's size*

The sensitivity of the results to the RVE's size or also the number of cells, n, was examined by comparing the predicted reduced stress–strain results. In order to be statistically representative, 20 random Voronoï honeycombs with the same relative density of .1 and with $\alpha = .5$ were generated and elementary volumes with a mean number of cells $n =$ 19, 28, 46, 65 and 100 were used to compute the reduced stress. Initially, the generated honeycombs contained, on average, 200 cells and elementary volumes were extracted (see Figure 12).

The results for the reduced stress are plotted against the strain for each value of n in Figure 13. The deviations between the results are reasonably small and hence, the size of the RVE was fixed to a minimum of 19 cells.

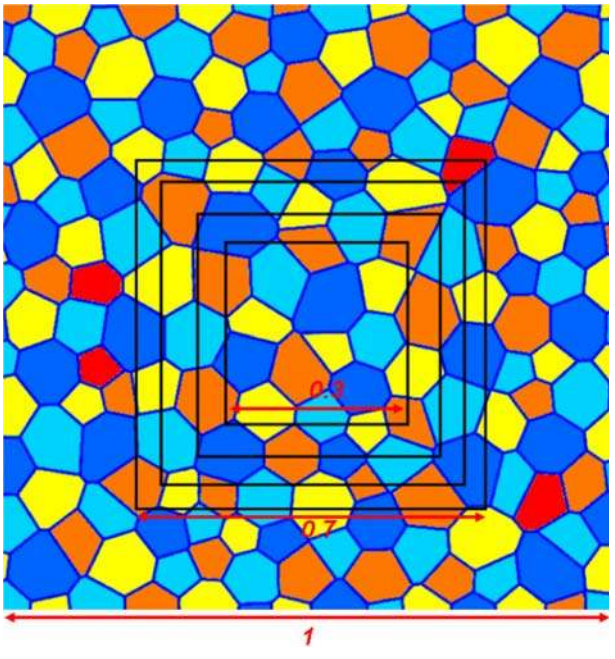

Figure 12. Elementary volumes extracted from an irregular Voronoı honeycomb containing 198 cells in order to determine the size of the RVE.

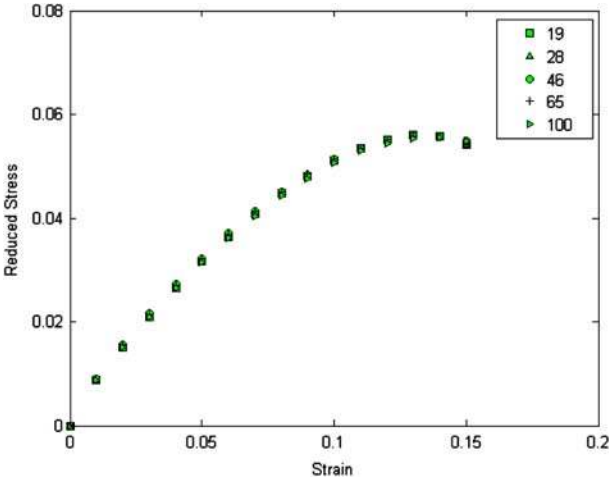

Figure 13. The influence of the number of cells in the honeycomb elementary volumes on the reduced stress–strain predictions.

4.4.2. The effect of the air

In the simulations shown above, the honeycombs' cells contained air. In order to eliminate the presence of the air inside the cells and leave only the foam's solid skeleton, all the elements of the FE mesh (i.e. triangles) containing only air were killed (removed). The killing process is simply performed by the means of the air's presence function; the elements in which this function is equal to one are removed (see Figure 14(a) and (b)).

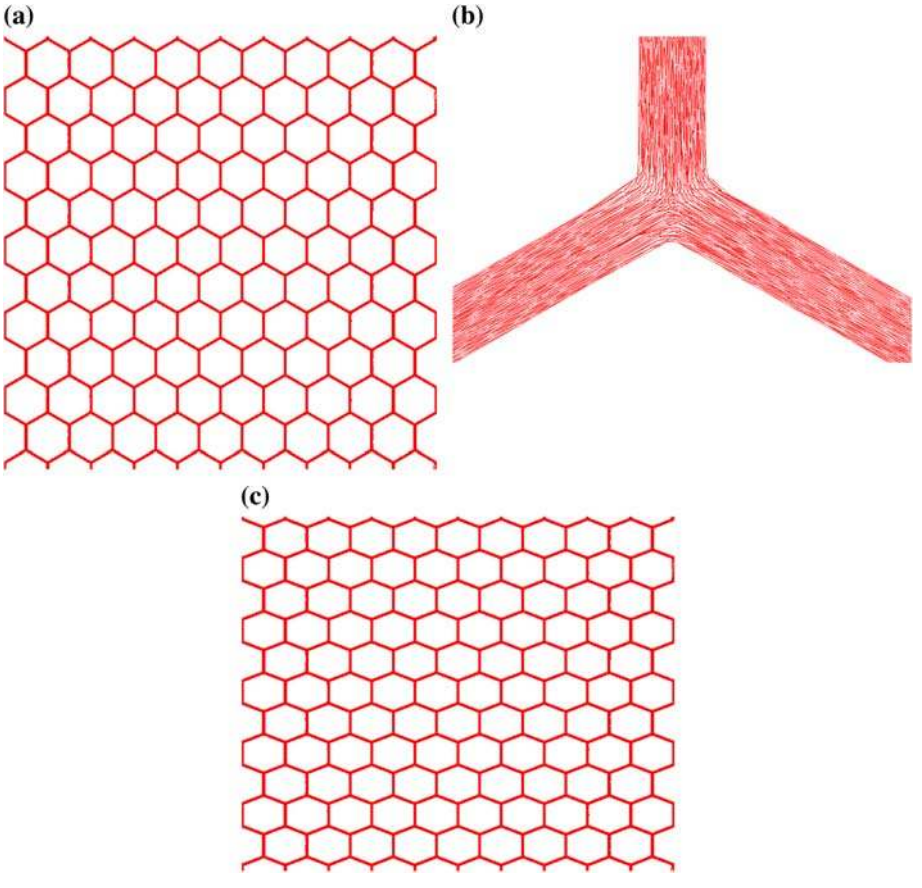

Figure 14. (a) The elastic solid skeleton of a regular Voronoı honeycomb with a relative density of .095 in its stable position, (b) a zoom at a triple junction showing the non-existence of mesh elements inside the cells and (c) the same honeycomb after 20% deformation.

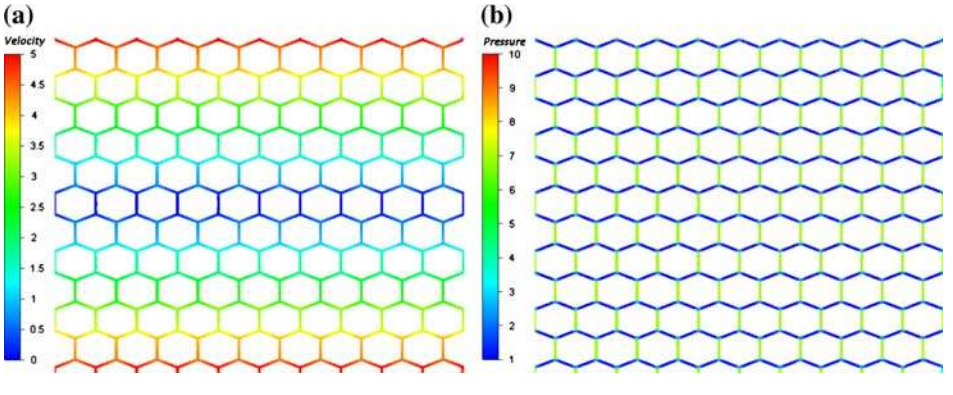

Figure 15. (a) The velocity of the solid skeleton at 20% deformation and (b) the pressure of the solid skeleton at 20% deformation.

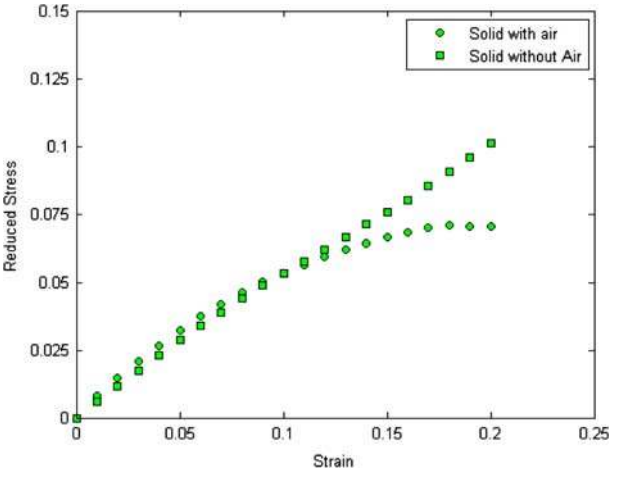

Figure 16. Comparison between the response of a solid skeleton with air inside the honeycomb's cells and without air.

As only the elastic solid skeleton is considered, our problem is now governed only by the solid Equation (40). A simulation up to 20% deformation of a regular Voronoï honeycomb with $\rho = .095$ was carried out and illustrated in Figure 14(c).

Figure 15 shows the norm of the velocity and the pressure of the Voronoï honeycomb at a strain of 0.2. We notice that the velocity is linear and symmetric in regards to the honeycomb's median plane which is normal since the honeycomb is periodic and since we considered frictionless contacts. The results show as well that the pressure on the solid edges that are parallel to the loading directions is the highest.

Moreover, we compared the reduced stress–strain curves of this Voronoï honeycomb (i.e. solid skeleton without air) and of the solid part of a honeycomb with the same relative density but with air inside its cells (see Figure 16). We notice that the two skeletons have approximately the same reduced stress values at strains lower than .12. Then, the one with air

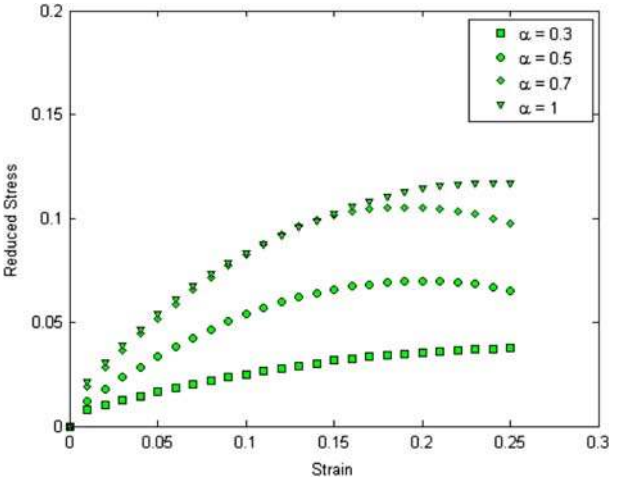

Figure 17. The influence of cell irregularity on the reduced stress–strain predictions.

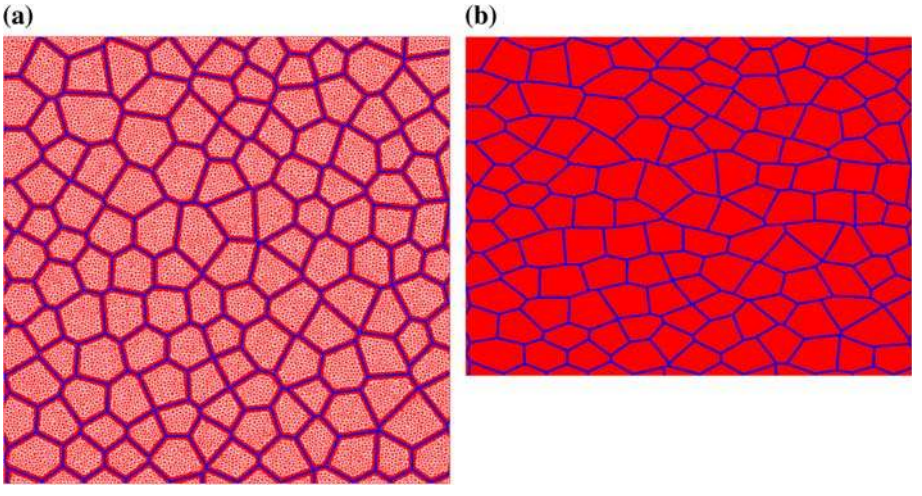

Figure 18. (a) The Voronoï honeycomb with $\alpha = .7$ and $\rho = .102$ in its undeformed state and the anisotropic meshing at the interfaces and (b) after 25% of biaxial compression.

reaches its plateau region and the one without air continues to follow a linear elastic behaviour. This yields that the air, or most precisely the air's pressure, encourages the elastic buckling of the solid skeleton and hence, the plateau region is reached earlier during the compression.

4.4.3. The effect of varying cell irregularity

Zhu et al. (2006) and Zhu and Windle (2002) studied the effect of α on the high strain compression of 2D Voronoï honeycombs and of open-cell foams. In their studies, where the air is not taken into consideration, they found that the compressive strength of a foam, defined as the maximum value of stress achieved during the simulated compression, decreases

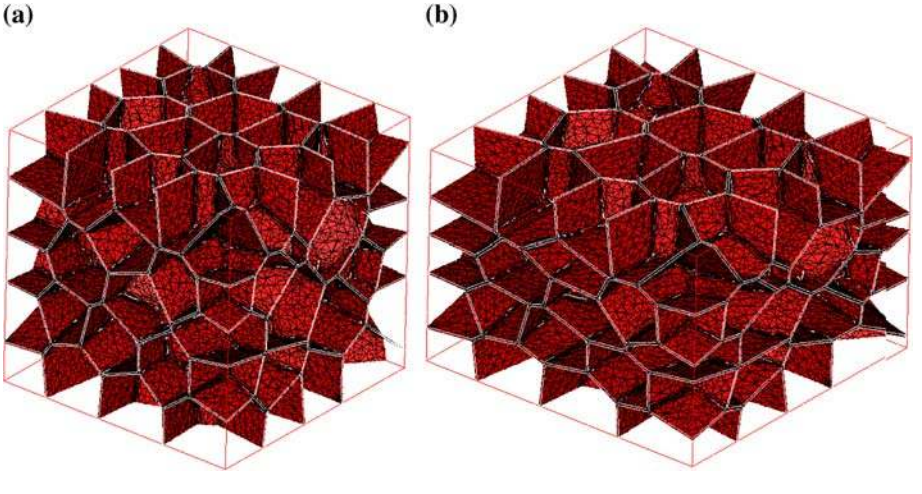

Figure 19. (a) The iso-zero of the level-set function defining a three-dimensional closed-cell foam made of 107 cells with a cell irregularity of .5 and a relative density of .1 at its initial state with the anisotropic remeshing and (b) the same foam after 30% deformation.

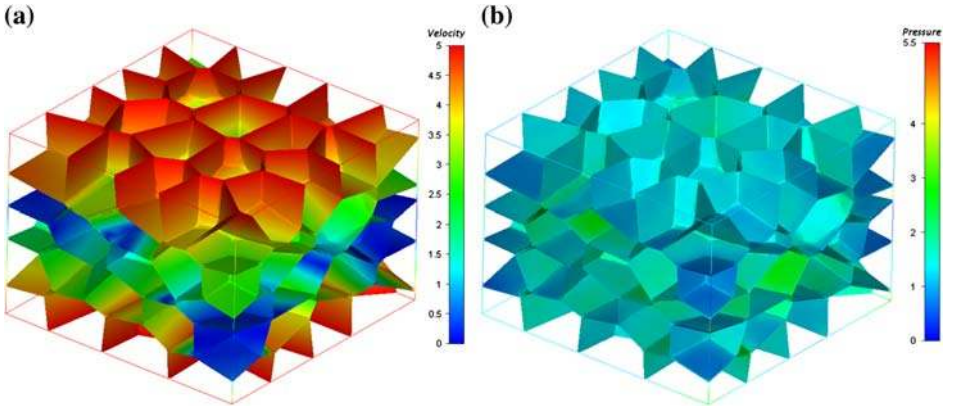

Figure 20. (a) The velocity's norm at 30% deformation of the closed-cell foam shown at the foam's interface and (b) the pressure at 30% deformation also shown at the foam's interface.

as the irregularity increases. We intend to use our FSI approach to also study the effect of varying cell irregularity on the compression of Voronoï honeycombs with air inside their cells. For this purpose, three Voronoï honeycombs with α values of .3, .5 and .7 were generated, and biaxial compressions were carried out up to 25% deformation. In Figure 17, the results with varying cell irregularity are compared along with the corresponding result for a regular hexagonal honeycomb.

Though the air is present inside the cells, our results also show that the foam's stress is reduced as the irregularity increases. This can be explained by the fact that the air's fraction inside the cells is equal for all the considered honeycombs and hence, the effect of the cell irregularity on the reduced stress remains the same.

Figure 18 illustrates an irregular Voronoï honeycomb with $\alpha = .7$ at its initial state and after 25% deformation.

4.4.4. Compression of a three-dimensional closed-cell foam

A three-dimensional closed-cell foam, made of 107 cells, with a cell irregularity of .5 and a relative density of .1 was generated in a unit cube. Anisotropic mesh adaptation was per-

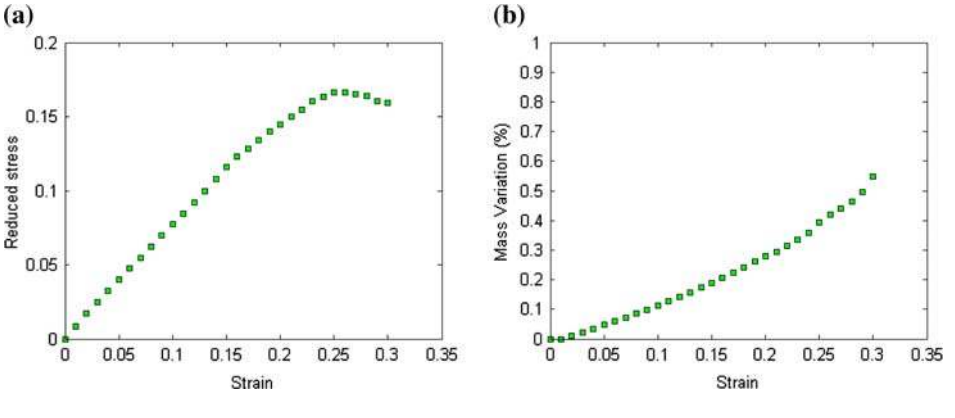

Figure 21. (a) The reduced stress/strain curve of the irregular closed-cell foam and (b) the variation of its mass.

formed in order to properly describe the foam. The resulting FE mesh is made of 349,659 nodes and 1,957,422 elements. Figure 19(a) illustrates the foam at its initial state defined by the iso-zero of its level-set function where the anisotropic mesh is shown. A biaxial compression up to 30% was performed by imposing velocities on the upper and lower boundaries of the domain (see Figure 19(b)).

The simulation was performed on 96 processors in 1 h and 12 min after the construction of the initial mesh. Figure 20 illustrates the velocity's norm and pressure on the interface of the foam (i.e. the iso-zero of the level-set function) at 30% deformation.

Figure 21 shows the reduced stress/strain curve of the closed-cell foam and its mass variation. The foam presents a linearly elastic behaviour before reaching a plateau region at about 23% of deformation; this is due to the beginning of the elastic buckling of the cells. Furthermore, the mass variation does not exceed .6% which is a very reasonable loss and proves that the foam's mass is conserved during the whole process.

5. Conclusion

A method to generate foam RVEs was detailed. It is based on the spreading of Laguerre cells describing the cellular structure. The cells were defined using a level-set approach and an efficient anisotropic mesh adaptation was used. Furthermore, a FE analysis has been presented to simulate the biaxial compression of elastic foams. The simulations were considered as an FSI problem, between a compressible elastic solid (i.e. the foam's skeleton) and a compressible fluid (i.e. the air), that was solved by a monolithic formulation in a Lagrangian framework. This kind of approach enabled us to study the air's effect on the foam's behaviour. Also, the effect of varying cell irregularity was studied and a compression of a three-dimensional closed-cell foam was performed. The results yielded that the honeycomb's stress reaches a plateau region earlier when the air is present inside the foam's cells and that it is reduced as the irregularity increases. Furthermore, the closed-cell foam presented a typical behaviour of elastic foams during compression, and the mass of the whole structure was conserved.

Acknowledgement

The present study is supported by the Rem3D® consortium. This support is gratefully acknowledged.

References

Almeida, R., Feijoo, R., Galeao, A., Padra, C., & Silva, R. (2000). Adaptive finite element computational fluid dynamics using an anisotropic error estimator. *Computer Methods in Applied Mechanics and Engineering, 182*, 379–400.

Appel, K., & Haken, W. (1976). Every planar map is four colorable. *Bulletin of the American Mathematical Society, 82*, 711–712.

Arnold, D., Brezzi, F., & Fortin, M. (1984). A stable finite element for the stokes equations. *Calcolo, 21*, 337–344.

Benabbou, A., Borouchaki, H., Laug, P., & Jian, L. (2009). Geometrical modeling of granular structures in two and three dimensions. Application to nanostructures. *International Journal for Numerical Methods in Engineering, 80*, 425–454.

Benabbou, A., Borouchaki, H., Laug, P., & Jian, L. (2010). Numerical modeling of nanostructured materials. *Finite Elements in Analysis and Design, 46*(1–2), 165–180.

Bernacki, M., Chastel, Y., Coupez, T., & Logé, R.E. (2008). Level set framework for the numerical modelling of primary recrystallization in polycrystalline materials. *Scripta Materialia, 58*, 1129–1132.

Bernacki, M., Resk, H., Coupez, T., & Logé, R.E. (2009). Finite element model of primary recrystallization in polycrystalline aggregates using a level set framework. *Modelling and Simulation in Materials Science and Engineering*, *17*, 064006.

Bernacki, M., Logé, R.E., & Coupez, T. (2011). Level set framework for the finite-element modelling of recrystallization and grain growth in polycrystalline materials. *Scripta Materialia, 64*, 525–528.

Brélaz, D. (1979). New methods to color the vertices of a graph. *Communications of the ACM, 22*, 251–256.

Coupez, T. (1996). *Stable-stabilized finite element for 3D forming calculation*. Internal report, Mines ParisTech.

Coupez, T., Digonnet, H., & Ducloux, R. (2000). Parallel meshing and remeshing: Dynamic load balancing of mesh-based applications on parallel. *Applied Mathematical Modelling, 25*, 153–175.

Digonnet, H., Silva, L., & Coupez, T. (2007). Cimlib: A fully parallel application for numerical simulations based on components assembly. *Materials Processing and Design; Modeling, Simulation and Applications; NUMIFORM '07; Proceedings of the 9th International Conference on Numerical Methods in Industrial*.

Franca, L., Nesliturk, A., & Stynes, M. (1998). On the stability of residual-free bubbles for convection diffusion problems and their approximation by a two-level finite element method. *Computer Methods in Applied Mechanics and Engineering, 166*, 35–49.

Gibson, L.J. & Ashby, M.F. (1997). *Cellular solids: Structure and properties* (2nd ed.). Cambridge: Cambridge University Press.

Glickenstein, D. (2007). A monotonicity property for weighted delaunay triangulations. *Discrete and Computational Geometry, 38*, 651–664.

Gruau, C. (2004). *Metric generation for anisotropic mesh adaptation, with numerical applications to material forming simulation*. PhD Thesis, Mines ParisTech, Sophia Antipolis.

Hachem, E. (2009). *Stabilized finite element method for heat transfer and turbulent flows inside industrial furnaces*. PhD Thesis, Mines ParisTech, Sophia Antipolis.

Hachem, E., Kloczko, T., Digonnet, H., & Coupez, T. (2012). Stabilized finite element solution to handle complex heat and fluid flows in industrial furnaces using the immersed volume method. *International Journal for Numerical Methods in Fluids,* 68(1), 99–121.

Hitti, K. (2011). *Direct numerical simulation of complex Representative Volume Elements (RVEs): Generation, Resolution and Homogenization.* PhD Thesis, Mines Paristech, Sophia Antipolis.

Hitti, K., Laure, P., Coupez, T., Silva, L., & Bernacki, M. (2012). Precise generation of complex statistical Representative Volume Elements (RVEs) in a finite element context. *Computational Materials Science, 61*, 224–238.

Imai, H., Iri, M., & Murota, K. (1985). Voronoi diagram in the Laguerre geometry and its applications. *SIAM Journal on Computing, 14*(1), 93–105.

Jang, W.-Y., Kraynik, A.M., & Kyriakides, S. (2008). On the microstructure of open-cell foams and its effect on elastic properties. *International Journal of Solids and Structures, 45*, 1845–1875.

Kubale, M. (2004). *Graph colorings*. Rhode Island: American Mathematical Society Providence.

Li, K., Gao, X.L., & Subhash, G. (2005). Effects of cell shape and cell wall thickness variations on the elastic properties of two-dimensional cellular solids. *International Journal of Solids and Structures, 42*, 1777–1795.

Li, K., Gao, X.-L., & Subhash, G. (2006). Effects of cell shape and strut cross-sectional area variations on the elastic properties of three-dimensional open-cell foams. *Journal of the Mechanics and Physics of Solids, 54*, 783–806.

Marchi, C.S., & Mortensen, A. (2001). Deformation of open-cell aluminum foam. *Acta Materialia, 49*, 3959–3969.

Mesri, Y., Zerguine, W., Digonnet, H., Silva, L., & Coupez, T. (2008). Dynamic parallel adaption for three dimensional unstructured meshes: Application to interface tracking. *Proceedings of the 17th International Meshing Roundtable,* 195–212.

Mills, N.J. (2007). The high strain mechanical response of the wet Kelvin model for open-cell foams. *International Journal of Solids and Structures, 44*(1), 51–65.

Mills, N.J., & Zhu, H.X. (1999). The high strain compression of closed-cell polymer foams. *Journal of the Mechanics and Physics of Solids, 47*, 669–695.

Resk, H., Delannay L., Bernacki, M., Coupez, T., & Logé, R.E. (2009). Adaptive mesh refinement and automatic remeshing in crystal plasticity finite element simulations. *Modelling and Simulation in Materials Science and Engineering, 17*, 075012.

Simone, A.E., & Gibson, L.J. (1998). Effects of solid distribution on the stiffness and strength of metallic foams. *Acta Materialia, 46*, 2139–2150.

Sun, Z., Logé, R.E., & Bernacki, M. (2010). 3D finite element model of semi-solid permeability in an equiaxed granular structure. *Computational Materials Science, 49*(1), 158–170.

Warren, W.E., & Kraynik, A.M. (1988). The linear elastic properties of open-cell foams. *Journal of Applied Mechanics, 55*, 341–346.

Warren, W.E., & Kraynik, A.M. (1997). Linear elastic behavior of a low-density Kelvin foam with open cells. *Journal of Applied Mechanics, 64*, 787–794.

Wismans, J.G.F., Govaert, L.E., & van Dommelen, J.A.W. (2010). X-ray computed tomography-based modeling of polymeric foams: The effect of finite element model size on the large strain response. *Journal of Polymer Science Part B: Polymer Physics, 48*, 1526–1534.

Wismans, J.G.F., van Dommelen, J.A.W., Govaert, L.E., & Meijer, H.E.H. (2010). X-ray computed tomography based modelling of polymer foams. *Materials Science Forum, 638–642*, 2761–2765.

Xu, T., & Li, M. (2009). Topological and statistical properties of a constrained Voronoi tessellation. *Philosophical Magazine, 89*, 349–374.

Zhang, J.L., & Lu, Z.X. (2007). Numerical modeling of the compression process of elastic open-cell foams. *Chinese Journal of Aeronautics,* 20, 215–222.

Zhu, H.X., Hobdell, J.R., & Windle, A.H. (2000). Effects of cell irregularity on the elastic properties of open-cell foams. *Acta Materialia, 48*, 4893–4900.

Zhu, H.X., Hobdell, J.R., & Windle, A.H. (2001). Effects of cell irregularity on the elastic properties of 2D Voronoi honeycombs. *Journal of the Mechanics and Physics of Solids, 49*, 857–870.

Zhu, H.X., Mills, N.J., & Knott, J.F. (1997). Analysis of the high strain compression of open-cell foams. *Journal of the Mechanics and Physics of Solids, 45*, 1875–1899.

Zhu, H.X., Thorpe, S.M., & Windle, A.H. (2006). The effect of cell irregularity on the high strain compression of 2D Voronoi honeycombs. *International Journal of Solids and Structures, 43*, 1061–1078.

Zhu, H.X., & Windle, A.H. (2002). Effects of cell irregularity on the high strain compression of open-cell foams. *Acta Materialia, 50*, 1041–1052.